Topologically Protected Twist Edge States for a Resonant Mechanical Laser-Beam Scanner

Julian Köpfler,[1,2,*] Tobias Frenzel,[2] Muamer Kadic,[1,2,3] Jörg Schmalian,[4,5] and Martin Wegener[1,2]

[1] *Institute of Nanotechnology, Karlsruhe Institute of Technology, Karlsruhe, Germany*

[2] *Institute of Applied Physics, Karlsruhe Institute of Technology, Karlsruhe, Germany*

[3] *FEMTO-ST, Université de Bourgogne Franche-Comté, Besançon, France*

[4] *Institute for Theoretical Condensed Matter Physics, Karlsruhe Institute of Technology, Karlsruhe, Germany*

[5] *Institute for Solid-State Physics, Karlsruhe Institute of Technology, Karlsruhe, Germany*

(Received 11 December 2018; revised manuscript received 16 January 2019; published 25 March 2019)

We design a one-dimensional chain of two different alternating three-dimensional elastic chiral unit cells. The chain's topological band gap, a result of the alternation of unit cells combined with their chirality and an effective mirror symmetry, guarantees a protected edge state, corresponding to a localized twist mode with an eigenfrequency inside the one-dimensional band gap. A small axial modulation at the one end of the beam can excite this resonant twist mode at the other end of the beam, via evanescent modes in the gap. The topological robustness of the edge state allows us to add a micromirror to the other end of the beam, turning the arrangement into a resonant mechanical laser-beam scanner. Its scalable operation frequency makes it attractive for applications.

DOI: 10.1103/PhysRevApplied.11.034059

I. INTRODUCTION

Electronic band gaps are the basis of semiconductor physics and today's information technology. Throughout the past three decades, the concept of band gaps has also extensively been applied to photonic [1–3] and phononic [4–6] systems to tailor bulk properties. Band gaps can additionally lead to interesting surface properties. Modes may exist at the surface of a band-gap material, at eigenfrequencies inside the band gap. In general, this situation is not at all guaranteed. However, it is guaranteed for a special class of band gaps called topological band gaps, for which the associated surface or edge modes are even robust against substantial perturbations [7–10]. Robust edge modes can also occur in the static case [11]. Theory has systematically classified the conditions for band gaps to be topological in nature for electronic, optical, and mechanical structures with periodicities in one, two, and three dimensions [12–14].

As far as potential applications of topological band gaps in photonics and phononics are concerned, the emphasis so far has been on unidirectionally propagating edge modes [15–22], analogous to the edge states in electronic quantum Hall systems in the presence of a static magnetic field [23,24]. In essence, these photonic and phononic studies aim at innovative robust waveguide architectures. In this paper, we aim at a different kind of application specifically based on topological band gaps, namely a resonant chiral edge state that converts the small axial motion induced by a piezoelectric actuator at the one end of a beam into a large rotation of a mirror at the other end, allowing us to scan a laser beam. This arrangement is illustrated in Fig. 1.

The paper is organized as follows. In Sec. II, we start the design process by using an analytical one-dimensional (1D) mass-spring model, which we solve to obtain overview "phase diagrams" for the Zak phase [25,26] of the relevant bands, which is crucial to determining whether or not the gap in between the bands is topological. The system resembles two Su-Schrieffer-Heeger (SSH) models [27], one for the longitudinal displacement in a beam and one for the twist. The two are chirally coupled via additional springs. We justify this model by the fact that the longitudinal (or pressure) and the twist mode on the one hand, and the two transverse (or shear) modes on the other, inhabit orthogonal subspaces according to micropolar continuum theory [28]. In Sec. III, we classify our system according to its symmetries. Within our model, the topological protection is due to a combination of time-reversal symmetry and a mirror symmetry, generalizing the classification of mechanical metamaterials [14]. As a result of the additional mirror symmetry, the topological state is characterized by a $\mathcal{Z}_2$ index that is related to the Berry phase of the 1D phononic band structure, i.e., to the Zak phase. In

*julian.koepfler@kit.edu

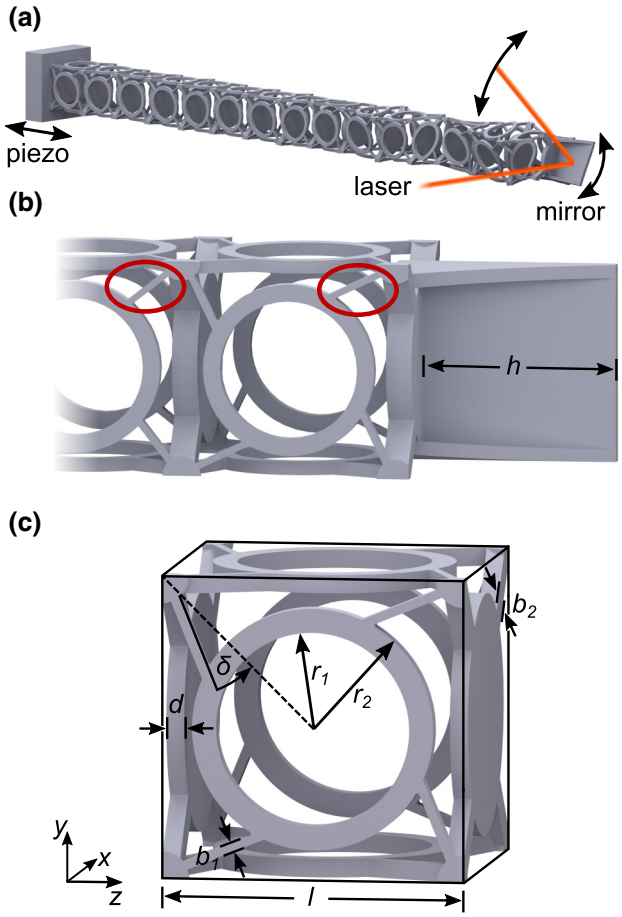

FIG. 1. (a) A designed elastic beam can convert the weak time-harmonic axial excitation at one end of the beam into the excitation of an edge mode at the other end. The edge mode exhibits a large twist motion or rotation. A micromirror fixed to the other end of the beam can thus deflect a laser beam. (b) A magnified view onto the end with the mirror. The required 1D topological band gap is accomplished by an alternation of two different 3D chiral cells. The two red ellipses highlight the subtle structural difference between the two neighboring cube cells. One of the cells is depicted in (c), together with relevant geometrical parameters. In particular, the angle δ controls the level of chirality. The cell becomes achiral for $\delta = 0$. Panel (c) has been adapted with permission from Ref. [31].

Sec. IV, we discuss the importance of the boundary conditions for the existence of protected edge states in such a mechanical topological system. In Sec. V, the results of the model are verified by numerical finite-element calculations for finite-size three-dimensional (3D) microstructures. The designed 3D microstructures are amenable to state-of-the-art 3D laser nanoprinting [29–31]. However, as shown by our calculations, low material losses are crucial to obtaining a notable resonant enhancement of the mirror rotation. Therefore, constituent materials other than the polymers commonly used in 3D laser nanoprinting today might be needed. Information on the polymer's material losses or potential alternative materials are not readily available at present, as pointed out when we conclude in Sec. VI.

II. THE ANALYTICAL MODEL

Our design approach, which is illustrated in Fig. 1, is inspired by recent experimental progress on 3D chiral micropolar metamaterials [31]. These artificial materials allow us to convert an axial push onto an elastic beam into a twisting of the beam. Notably, this conversion is strictly forbidden in ordinary Cauchy continuum elasticity [32]. One can use such a micropolar beam, as it is, to convert an axial time-harmonic excitation at one end of the beam, e.g., one induced by a piezoelectric actuator, into a rotation of a mirror fixed to the other end, to thereby obtain a laser scanner. However, it is notoriously difficult to obtain large actuation amplitudes at high frequencies. Therefore, it is highly desirable to introduce a suitable resonance with a high quality factor into this arrangement. Our approach is to design a resonant edge state at the other end of the beam and weakly couple to it via evanescent modes in the band gap. As pointed out in Sec. I, the existence of such an edge state with an eigenfrequency inside the band gap is guaranteed if and only if we design for a 1D topological band gap of the beam.

An elastic beam with a finite cross section generally supports four "acoustic" modes emerging from the Brillouin zone center: two shear modes, one longitudinal pressure mode, and one twist mode. In the presence of chirality, the latter two are mixed modes, in accordance with micropolar continuum theory. This mixing is at the heart of the axial-strain-to-twist conversion at which we are aiming. In contrast, the chiral shear modes (or "chiral phonons" [33]) are not of interest here. Fortunately, our analytical analysis of the micropolar Eringen equations of motion [28] for 3D continuous media shows that the two pairs of modes live in orthogonal subspaces. We can therefore build our model onto the pressurelike and twistlike modes only. In the numerical analysis of 3D microstructures to be presented in Sec. V, all modes are automatically included. The good agreement between analytics and numerics will provide an additional *a posteriori* justification for using the simple analytical model.

Furthermore, it is known that 1D topological band gaps in mechanics can be obtained via a "diatomic basis" (also see Refs. [14,34–37]), analogous to the electronic Su-Schrieffer-Heeger (SSH) model [27]. Thus, we consider a periodic alternation of two slightly different chiral 3D unit cells, as shown in Fig. 2(a). We reduce the arrangement to a 1D mass-spring model [Fig. 2(b)] with four coupled degrees of freedom (DOF) per lattice site i, i.e., its longitudinal displacements $u_{i,\mathrm{a}}$ and $u_{i,\mathrm{b}}$ and its axial rotations $\varphi_{i,\mathrm{a}}$ and $\varphi_{i,\mathrm{b}}$ at the sublattice sites a and b respectively. Similar models have recently been used to study the band structure of chiral metastructures [38,39]. The equations of motion

for the two DOF of sublattice site a in unit cell i read as follows:

$$m_{\mathrm{a}}\ddot{u}_{i,\mathrm{a}} = D_1^{uu}\left(u_{i,\mathrm{b}} - u_{i,\mathrm{a}}\right) + D_2^{uu}\left(u_{i-1,\mathrm{b}} - u_{i,\mathrm{a}}\right) + D_1^{u\varphi}\left(\varphi_{i,\mathrm{b}} - \varphi_{i,\mathrm{a}}\right) + D_2^{u\varphi}\left(\varphi_{i-1,\mathrm{b}} - \varphi_{i,\mathrm{a}}\right), \quad (1)$$

$$j_{\mathrm{a}}\ddot{\varphi}_{i,\mathrm{a}} = D_1^{\varphi\varphi}\left(\varphi_{i,\mathrm{b}} - \varphi_{i,\mathrm{a}}\right) + D_2^{\varphi\varphi}\left(\varphi_{i-1,\mathrm{b}} - \varphi_{i,\mathrm{a}}\right) + D_1^{\varphi u}\left(u_{i,\mathrm{b}} - u_{i,\mathrm{a}}\right) + D_2^{u\varphi}\left(u_{i-1,\mathrm{b}} - u_{i,\mathrm{a}}\right), \quad (2)$$

where m_a and j_a are the mass and the moment of inertia of the element at sublattice site a, respectively. The intracell (intercell) longitudinal and torsional spring constants are denoted as $D_{1(2)}^{uu}$ and $D_{1(2)}^{\varphi\varphi}$, respectively. The effective parameters $D_{1(2)}^{u\varphi}$ and $D_{1(2)}^{\varphi u}$ represent the intracell (intercell) coupling between the longitudinal displacement and the rotation. Due to the symmetry of the acting forces, we have $D_{1(2)}^{u\varphi} = D_{1(2)}^{\varphi u}$. By analogy, two equations can be derived for sublattice site b. Fourier transforming the four equations of motion with respect to space and time leads to the following eigenequation:

$$\omega_{k,n}^2 \mathbf{u}_k^{(n)} = D_k \mathbf{u}_k^{(n)}, \quad (3)$$

in which

$$\mathbf{u}_k^{(n)} = \left(\sqrt{m_{\mathrm{a}}}u_{k,\mathrm{a}}^{(n)}, \sqrt{m_{\mathrm{b}}}u_{k,\mathrm{b}}^{(n)}, \sqrt{j_{\mathrm{a}}}\varphi_{k,\mathrm{a}}^{(n)}\sqrt{j_{\mathrm{b}}}\varphi_{k,\mathrm{b}}^{(n)}\right)^T, \quad (4)$$

$$D_k = \begin{pmatrix} \frac{D_1^{uu} + D_2^{uu}}{m_{\mathrm{a}}} & \frac{-D_1^{uu} - D_2^{uu}e^{-\mathrm{i}ka}}{\sqrt{m_{\mathrm{a}}m_{\mathrm{b}}}} & \frac{D_1^{u\varphi} + D_2^{u\varphi}}{\sqrt{m_{\mathrm{a}}j_{\mathrm{a}}}} & \frac{-D_1^{u\varphi} - D_2^{u\varphi}e^{-\mathrm{i}ka}}{\sqrt{m_{\mathrm{a}}j_{\mathrm{b}}}} \\ \frac{-D_1^{uu} - D_2^{uu}e^{\mathrm{i}ka}}{\sqrt{m_{\mathrm{a}}m_{\mathrm{b}}}} & \frac{D_1^{uu} + D_2^{uu}}{m_{\mathrm{b}}} & \frac{-D_1^{u\varphi} - D_2^{u\varphi}e^{\mathrm{i}ka}}{\sqrt{m_{\mathrm{b}}j_{\mathrm{a}}}} & \frac{D_1^{u\varphi} + D_2^{u\varphi}}{\sqrt{m_{\mathrm{b}}j_{\mathrm{b}}}} \\ \frac{D_1^{u\varphi} + D_2^{u\varphi}}{\sqrt{m_{\mathrm{a}}j_{\mathrm{a}}}} & \frac{-D_1^{u\varphi} - D_2^{u\varphi}e^{-\mathrm{i}ka}}{\sqrt{m_{\mathrm{b}}j_{\mathrm{a}}}} & \frac{D_1^{\varphi\varphi} + D_2^{\varphi\varphi}}{j_{\mathrm{a}}} & \frac{-D_1^{\varphi\varphi} - D_2^{\varphi\varphi}e^{-\mathrm{i}ka}}{\sqrt{j_{\mathrm{a}}j_{\mathrm{b}}}} \\ \frac{-D_1^{u\varphi} - D_2^{u\varphi}e^{\mathrm{i}ka}}{\sqrt{m_{\mathrm{a}}j_{\mathrm{b}}}} & \frac{D_1^{u\varphi} + D_2^{u\varphi}}{\sqrt{m_{\mathrm{b}}j_{\mathrm{b}}}} & \frac{-D_1^{\varphi\varphi} - D_2^{\varphi\varphi}e^{\mathrm{i}ka}}{\sqrt{j_{\mathrm{a}}j_{\mathrm{b}}}} & \frac{D_1^{\varphi\varphi} + D_2^{\varphi\varphi}}{j_{\mathrm{b}}} \end{pmatrix}, \quad (5)$$

where k is the wave number, n is the band index, $\omega_{k,n}$ is the angular frequency, D_k is the dynamical matrix, and a is the lattice constant of the mass-spring chain. Here, the band index runs from $n = 1$ to 4, resulting from the two longitudinal and the two rotational DOF per unit cell. The band structures for exemplary choices of coupling constants are depicted in Figs. 3(a) and 3(b). A band gap between the second and third band is induced by an anticrossing between the upper acoustic and the lower optical band.

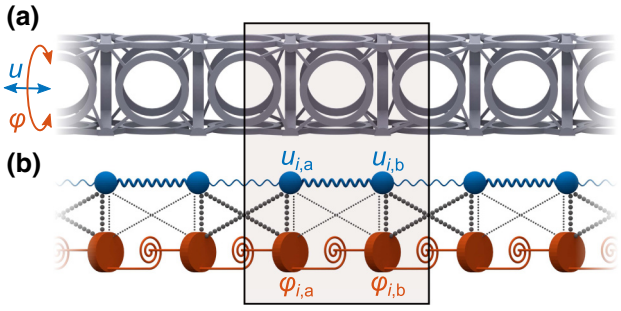

FIG. 2. (a) The alternation of 3D cubic chiral cells as in Fig. 1(b). We map this complex microstructure onto two coupled Su-Schrieffer-Heeger (SSH) models for the displacement u and the twist angle φ [Eqs. (1) and (2)]. (b) The chiral coupling is indicated by the gray dotted lines. The amplitudes of the coupling coefficients are illustrated qualitatively by the different Hooke's springs. The grayish box shows the unit-cell convention used in this work.

III. TOPOLOGICAL CLASSIFICATION

In order to evaluate the system's topology, the eigenvectors $\mathbf{u}_k^{(n)}$, which contain the complex, wave number-dependent amplitudes of the four DOF, are calculated for a given matrix D_k. The topological index of a band n is then given by the accumulated Berry phase over the 1D Brillouin zone, i.e., by the Zak phase [26]

$$\gamma^{(n)} = \mathrm{i}\int_{-\pi/a}^{\pi/a} \langle \mathbf{u}_k^{(n)} | \partial_k \mathbf{u}_k^{(n)} \rangle = -\mathrm{Im}\sum_{k_i=-\pi/a}^{\pi/a}\sum_{c=1}^{4} u_{k_i,c}^{(n)*} u_{k_i+\Delta k,c}^{(n)}. \quad (6)$$

In general, the Zak phase of the considered mass-spring model is *not* quantized. However, we find that the Zak phase of the four lowest bands is quantized if the masses

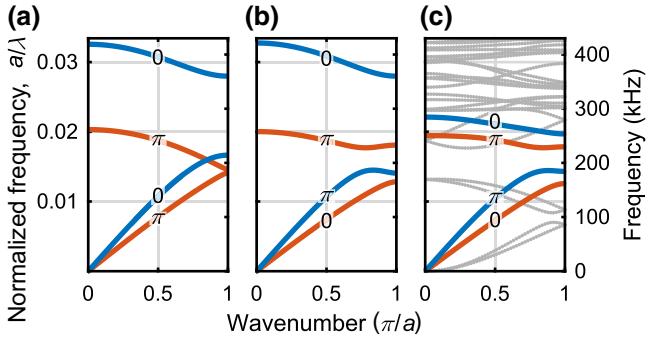

FIG. 3. (a) The band structure of the mass-spring model without chiral coupling ($D_1^{u\varphi} = D_2^{u\varphi} = 0$) and (b) with chiral coupling ($D_1^{u\varphi} \neq 0; D_2^{u\varphi} \neq 0$). In (a), the red and blue lines correspond to the rotational and longitudinally polarized (pressure) bands, respectively. Each of the band pairs is separated by a band gap—which, however, is very small for the rotational bands and not visible within the line width. For the coupled case in (b), individual bands exhibit mixed rotational-longitudinal modes. The calculated associated Zak phases are indicated. The resulting band gap between the second and third band in (b) is topologically nontrivial. The normalized coupling parameters are as follows: $\tilde{D}_1^{uu} = D_1^{uu}a^2/m = 1459$ N m/kg, $\tilde{D}_2^{uu} = 0.354\tilde{D}_1^{uu}$, $\tilde{D}_1^{\varphi\varphi} = D_1^{\varphi\varphi}a^2/j = 370$ N m/kg, $\tilde{D}_2^{\varphi\varphi} = 1.081\tilde{D}_1^{\varphi\varphi}$, $\tilde{D}_1^{u\varphi} = D_1^{u\varphi}a^2/\sqrt{mj} = 23.3$ N m/kg, and $\tilde{D}_2^{u\varphi} = 6\tilde{D}_1^{u\varphi}$. (c) The band structure as obtained from finite-element calculations of the microstructure shown in Fig. 2(a). The lower red and blue bands are as in (b): their Zak phases agree with those in (b). The Zak phases have been obtained from the underlying modes' parity (see Fig. 6). The bands shown in gray are shear modes (which do not couple to the colored bands), third or higher back-folded longitudinal or rotational bands, or originate from local resonances within the cells at frequencies above the colored bands. The structure parameters are as follows: $r_1 = 0.32l$, $r_2 = 0.4l$, $d = 0.06l$, $b_1 = 0.098l$, $b_2 = 0.03l$, $\delta_1 = 7.2°$, and $\delta_2 = 19.6°$ [according to Fig. 1(c)]. The frequency scale on the right-hand side corresponds to a cube-cell size of $l = a/2 = 150$ μm.

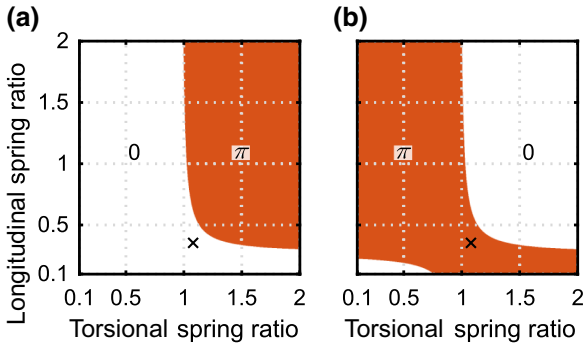

FIG. 4. Topological "phase diagrams" of the mass-spring model illustrated in Fig. 2 for (a) the first and (b) the second longitudinal-torsional band. A trivial phase with a Zak phase of $\gamma = 0$ is shown in white and a nontrivial phase with $\gamma = \pi$ is shown in red. On the horizontal axis, we vary the torsional spring-constant ratio ($D_2^{\varphi\varphi}/D_1^{\varphi\varphi}$), and on the vertical axis, we vary the longitudinal spring-constant ratio (D_2^{uu}/D_1^{uu}) for constant chiral coupling parameters (see Fig. 3). D_1^{uu} and $D_1^{\varphi\varphi}$ are kept constant while D_2^{uu} and $D_2^{\varphi\varphi}$ are varied. Due to the SSH mechanism combined with the anticrossing, either the first or the second band is nontrivial for most of the considered configurations. Thus, the band gap has a nontrivial topology over a wide parameter range. Only for very small ratios of the spring constants are both the first and the second band in the trivial phase. The parameter configuration that reproduces the microstructure's band structure [compare Figs. 3(b) and 3(c)] is highlighted by a black cross.

and moments of inertia of the two dissimilar sublattice sites are equal ($m_a = m_b = m$ and $j_a = j_b = j$). This condition is a prerequisite for topologically nontrivial states. Furthermore, this condition establishes a mirror symmetry of the mass distribution with respect to the center of the unit cell. In this case, both the upper left and lower right 2×2 blocks of the dynamical matrix in Eq. (5) resemble the Hamiltonian of the SSH model, one for the longitudinal and one for the rotational DOF Thereby, the off-diagonal 2×2 blocks represent the chiral coupling between these two subsystems. The quantized Zak phase is a $\mathcal{Z}_2$ topological invariant. This means that it is only defined up to integer multiples of 2π. Hence, it can only assume the nonequivalent values 0 or π. The band gap's topological index

$$\nu = \frac{1}{2}\left[1 - \exp\left(\mathrm{i}\sum_n{}' \gamma^{(n)}\right)\right] \tag{7}$$

is determined by the sum $\sum_n{}' \gamma^{(n)}$. The prime emphasizes that the sum runs over the Zak phases of the bands below the band gap. For classical waves, the relation between the bands' Zak phases, the topological index of the band gap, and the existence of edge modes has been discussed in Ref. [40]. To obtain the topological "phase diagrams" shown in Fig. 4, we evaluate the Zak phase of the bands for a sweep of the spring constants. The first band has a Zak phase as expected from the SSH model. Typically, the first band's modes are twist dominated and thus the band has a nontrivial phase for $D_2^{\varphi\varphi} > D_1^{\varphi\varphi}$. Only for a small longitudinal spring constant D_2^{uu} (with $D_2^{uu} < D_1^{uu}$) can the influence of the longitudinal modes shift the phase to trivial. The Zak phase of the second band is affected by the anticrossing [cf., Fig. 3(b)]. The part of the second band close to the Brillouin-zone boundary originally emerges from the first optical band, which has the same topological phase as the first acoustic band, according to the SSH mechanism [see Fig. 3(a)]. As a result, the second band inherits the inverted phase of the first band, so that either the first or the second band is topologically nontrivial for most configurations. This provides a topological band gap over a wide parameter range. Only if both D_2^{uu} and $D_2^{\varphi\varphi}$ are very small, no anticrossing occurs, such that the first and the second band can be simultaneously in the trivial phase.

Notably, the Zak phase is not gauge invariant. This can be seen easily for the simple mechanical SSH model: A shift of the unit cell by half a lattice constant effectively interchanges the inter- and intracell spring constants, corresponding to a topological phase transition with a change in the bands' Zak phase from 0 to π or vice versa. However, despite the absence of gauge invariance, the existence of a topological edge state of a finite system is still uniquely determined. Here, the choice of the system's boundary determines the choice of the unit cell and fixes the Zak phase of the individual bands. In other words, we can evoke or eliminate an edge state by cutting the 1D mass-spring chain at a proper position.

The fundamental reason for the quantization of the Zak phase is the presence of the symmetries for the given dynamical matrix D_k or, more generally, for the continuum operator $\hat{D}_k$. The operator is Hermitian ($\hat{D}_k^\dagger = \hat{D}_k$) and as all elastic constants are real valued, $\hat{D}^T_{-k} = \hat{D}_k$ holds true. Therefore, an antiunitary operator exists, $\hat{\theta} = \hat{U}\mathcal{K}$, that is given by the product of a unitary operator $\hat{U}$ and a complex conjugation $\mathcal{K}$, with $\hat{\theta}^2 = +1$, commuting with $\hat{D}_k$. This symmetry is analogous to the ordinary bosonic time-reversal symmetry of a quantum-mechanical Hamiltonian. Following the Altland-Zirnbauer classification [41], an additional crystalline symmetry has to be present in order to obtain topologically nontrivial states in a 1D system. In our case, this additional symmetry is given by the mirror-symmetric distribution of mass density inside the diatomic unit cell. This symmetry is exact for the simple model discussed in the preceding section. It is approximate for the 1D chain of 3D microstructured unit cells to be discussed below. Thus, we can find a symmetry operator $\hat{P}$, fulfilling

$$\hat{P}\hat{D}_k\hat{P}^{-1} = \hat{D}_{-k}. \tag{8}$$

For the discussed analytical model with the dynamical matrix D_k of Eq. (5), this symmetry operator reads as follows:

$$\hat{P} = \sigma_0 \otimes \sigma_x = \begin{pmatrix} 0 & 1 & 0 & 0 \\ 1 & 0 & 0 & 0 \\ 0 & 0 & 0 & 1 \\ 0 & 0 & 1 & 0 \end{pmatrix}, \tag{9}$$

with the identity matrix σ_0 and the Pauli matrix σ_x. With this symmetry operator obeying Eq. (8), the system is classified by a topological $\mathcal{Z}_2$ index, i.e., the quantized Zak phase. At $k = 0$ and $k = \pi/a$, the operators $\hat{D}_k$ and $\hat{P}$ share eigenfunctions and we obtain

$$\begin{aligned} \hat{P}\mathbf{u}^{(n)}_{k=0} &= p_0^{(n)}\mathbf{u}^{(n)}_{k=0}, \\ \hat{P}\mathbf{u}^{(n)}_{k=\pi/a} &= p_\pi^{(n)}\mathbf{u}^{(n)}_{k=\pi/a}, \end{aligned} \tag{10}$$

where the two parity eigenvalues $p_0^{(n)}$ and $p_\pi^{(n)}$ are $+1$ (-1) for symmetric (antisymmetric) displacement and rotation with respect to the center of the unit cell and thus for an acoustic (optical) mode. It can be shown that it is possible to directly deduce the Zak phase of a band by simply regarding the parity eigenvalues. If the parity of a band's eigenvectors is the same at the center and boundary of the Brillouin zone ($p_0^{(n)} = p_\pi^{(n)}$), the band's topology is trivial. If the parity is different ($p_0^{(n)} \neq p_\pi^{(n)}$), the band is nontrivial, i.e., $\exp(\mathrm{i}\gamma^{(n)}) = p_0^{(n)} p_\pi^{(n)}$. This fact is commonly referred to as band inversion. It can be used to determine the Zak phases for bands of the mass-spring system as well as for the bands of the microstructure, as shown in Fig. 6.

IV. THE ROLE OF BOUNDARY CONDITIONS

Not only the chain termination but also the boundary conditions imposed on a finite 1D mechanical system are of fundamental importance for the existence of topologically protected edge states [42]. In contrast to systems with nonspatial global symmetries, such as particle-hole symmetry, the topological protection of the considered mechanical edge states is guaranteed by a spatial symmetry. Spatial symmetries can be easily violated by cutting the originally infinitely periodic system, thereby losing the topological protection (for a recent discussion in the context of electronic systems, see Refs. [43] and [44]). To investigate this aspect, we study the eigenmodes and eigenfrequencies of a *finite* version of our mass-spring chain [Eqs. (1) and (2)] for free and fixed boundaries, respectively. We find that the guarantee for the existence of edge

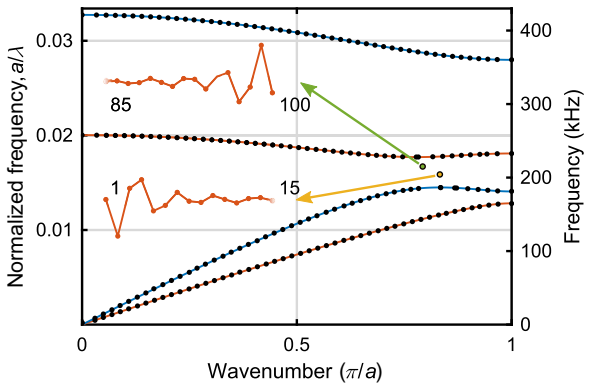

FIG. 5. The eigenfrequencies (black dots) of a finite-length mass-spring chain (cf., Fig. 2) with 100 lattice sites. The left boundary of the chain is fixed. The right boundary is open but approximates a fixed end by an additional mass $m_f = 2m$ (moment of inertia $j_f = 2j$) of the last element. The colored solid curves are identical to those in Fig. 3(b), with the same color coding. For the finite chain, the wave number of each eigenmode is obtained by a Fourier transformation of the spatial amplitude. Two edge modes with frequencies inside the band gap are found (green and yellow dots). The insets illustrate the corresponding twist amplitudes for the right end (left end) edge mode for the last (first) 15 lattice sites.

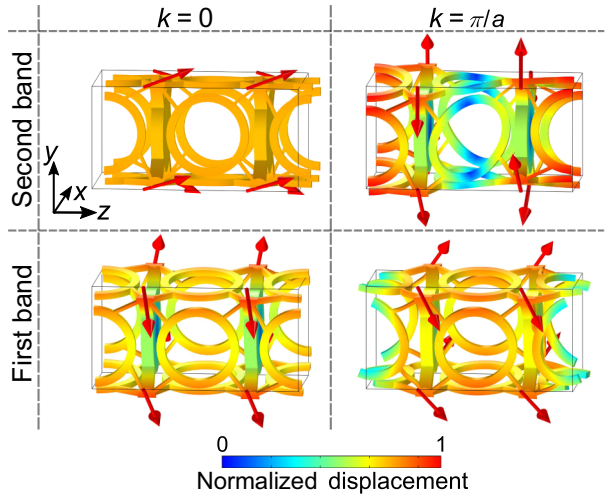

FIG. 6. The eigenmodes of the first and second longitudinal-torsional bands at the center (wave number $k = 0$) and the boundary ($k = \pm\pi/a$) of the first Brillouin zone. The red arrows show the displacement at the corners of the plates oriented along the z axis. For the first band, the two plates in the unit cell are symmetrically displaced at both, $k = 0$ and $k = \pm\pi/a$. This behavior indicates a trivial topology. For the second band, the plates are symmetrically displaced at $k = 0$ but antisymmetrically displaced at $k = \pm\pi/a$. This difference in parity, also called band inversion, indicates a nontrivial topology of the band.

states for a topologically nontrivial system only holds true for fixed boundary conditions. A fixed boundary corresponds to an additional infinite mass at the boundary. In the case of free (or open) boundary conditions, no protected edge states can be obtained, neither for a topologically trivial nor for a nontrivial configuration. However, by adding an increased mass to the final element of the open end of the chain, a fixed end can be approximated very well. Here, topological robustness helps in that the choice of this additional mass is not critical at all. Even for an only slightly increased mass, the eigenfrequency of the emerging edge state lies closely below the upper band edge and moves to the band gap's center frequency as the mass increases toward infinity. Figure 5 shows the eigenfrequencies (black dots) of a finite chain and the emerging edge modes (colored dots) for such a configuration with a free boundary and increased mass at one end of the chain. The solid red and blue curves are the bands of a fictitious infinitely long chain, as already shown in Fig. 3(b), which agree well with the eigenfrequencies of the finite-length chain. Snapshots of the two edge modes of the finite chain are illustrated by the two insets.

V. MICROSTRUCTURE

The envisioned microstructure has already been depicted in Fig. 1 and has briefly been discussed in Sec. I. Its purpose is to convert the axial excitation at one end of the beam, e.g., using a piezoelectric actuator, to a large-amplitude twist motion at the other end. This twist leads to a rotation of an attached small mirror (an additional mass). A laser beam reflected by this mirror will show an angular motion. This function corresponds to a resonant laser-beam scanner. The analytical results of the simple model presented in the preceding section help us to gain an overview and to specify the geometrical parameters of this microstructure. In this section, we discuss the numerical approach as well as the numerical results.

The constituent material is treated as a linear elastic Cauchy continuum. The resulting equations are solved numerically by a finite-element approach implemented in the commercial COMSOL multiphysics software package. We assume a real part of the Young's modulus of $E' = 2$ GPa, a Poisson's ratio of 0.4, and a mass density of $\rho = 1150$ kg/m^3. We calculate the band structures [e.g., Fig. 3(c)] for fictitious infinitely long microstructure chains by imposing periodic Floquet-Bloch boundary conditions onto the sides of the unit cell facing in the $\pm z$ direction, while using free (or open) boundaries at all other sides. We optimize the geometry of the two different 3D chiral elastic cube cells (cf., Fig. 1) to obtain a large topological band gap. The Zak phases of the bands, and thereby the topology of the band gap, are determined via the eigenmodes' parity, as shown in Fig. 6. Subsequently, we calculate the eigenfrequencies for a finite chain consisting of 15 chiral cube cells with a mirror plate attached to the loose right end. On the left end, we imply fixed boundary conditions. These boundary conditions correspond to the ones also discussed in Sec. IV. As discussed there, two edge states with frequencies inside the topological band gap, one for the left end and one for the right end, are found.

In Fig. 7(a), we show resonance plots, i.e., the squared normalized twist amplitude versus the excitation frequency. Here, the azimuthal component of the displacement vector on the right end is divided by the axial component of the displacement vector corresponding to the excitation on the left end. A squared normalized twist amplitude of 100 therefore corresponds to a resonant enhancement of the twist motion by a factor of 10. Enhancements as large as 240 are obtained in Fig. 7(a). Panel (b) shows snapshots of the displacement field for the four indicated resonances, 1, 2, 3, and 4. For other excitation frequencies in the band gap, the displacement field exhibits an exponential decay away from the left-hand side, as expected for evanescent modes (not depicted). Here, we have used a frequency-domain approach with a time-harmonic longitudinal excitation on the left end. The edge mode on the right end exhibits a strong twist motion of the last cubic cell. This finding confirms that this edge mode can indeed be excited from the other side via evanescent modes in the band gap. Thus, the structure provides the desired resonant conversion from longitudinal to twist actuation and can be used as a resonant laser-beam scanner. The

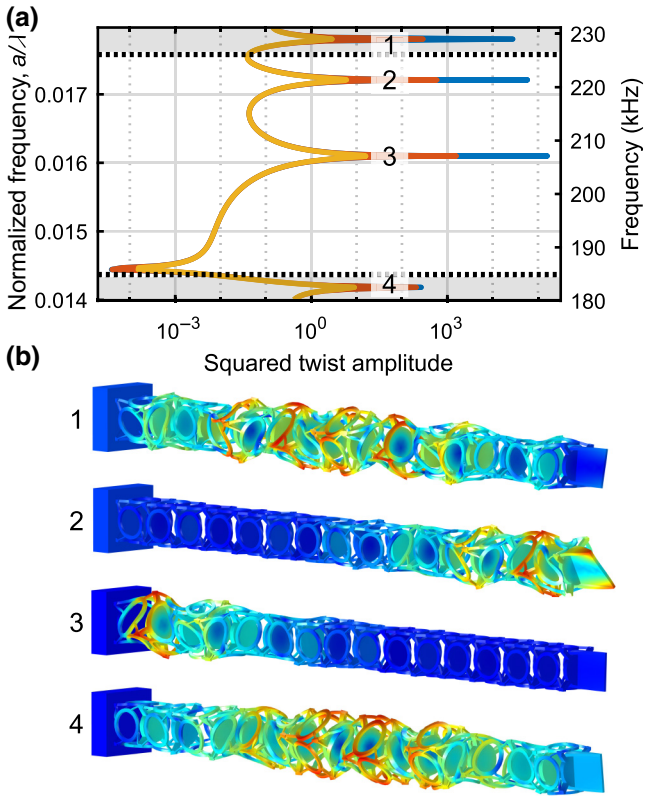

FIG. 7. (a) The normalized squared twist amplitude (on a logarithmic scale) versus the excitation frequency for three different ratios of the imaginary to the real part of the constituent material's Young's modulus E''/E': 2.5×10^{-5} (blue), 2.5×10^{-4} (red), and 2.5×10^{-3} (yellow). For unity normalized twist amplitude, the azimuthal component of the displacement vector has the same length as the axial component of the displacement vector corresponding to the excitation on the left end. (b) Snapshots of the displacement fields for the four resonances, 1, 2, 3, and 4, indicated in panel (a). Resonances 2 and 3 correspond to edge modes. Mode 2 is the one of interest in this paper (see also Fig. 1). The displacement fields, which are computed within the linear elastic regime, have been exaggerated for clarity.

system's operation frequency can be easily scaled, as it is inversely proportional to the cube cell size l. For an exemplary cell size of $l = 150$ μm, the resonance frequency is approximately 221 kHz. To study how material losses might influence the resonances and the connected maximum accessible rotation angles of the mirror, the calculations are performed for a finite imaginary part of the constituent material's Young's modulus, E''. The real part E' is fixed to $E' = 2$ GPa (see above). The colors blue, red, and yellow correspond to ratios E''/E' equal to 2.5×10^{-5}, 2.5×10^{-4}, and 2.5×10^{-3}, respectively. The associated quality factors of the resonance are $Q \approx 4 \times 10^4$, 4×10^3, and 4×10^2. Obviously, it is of the utmost importance to obtain small internal material losses in experiments. For the yellow curve, essentially no enhancement is left. The final optimization of the architecture depends on the material losses. In particular, the overall length of the beam has to be adjusted according to the actual material losses, i.e., according to the ratio E''/E'.

VI. CONCLUSION

We present a potential application of topological band gaps and corresponding topologically protected edge states in classical mechanics. The designed resonant laser-beam scanner additionally specifically exploits the chirality of the 3D unit cells of which the 1D chain of alternating cells is composed. This aspect requires chiral micropolar metamaterial unit cells, which have been realized experimentally in polymer form only recently. The quality factor of the edge-state resonance, and hence the enhancement of the twist motion, will eventually be limited by elastic material losses in experiments. To minimize these material losses and to optimize the microstructure accordingly presents a challenge for future experiments.

ACKNOWLEDGMENTS

We acknowledge support by the Virtual Materials Design (VIRTMAT) project of KIT, the Helmholtz Program Science and Technology of Nanosystems (STN), the Karlsruhe School of Optics & Photonics (KSOP), and the Excellence Cluster 3D Matter Made to Order (3DMM2O). M.K. acknowledges support by the EIPHI Graduate School (Contract "ANR-17-EURE-0002") and the French Investissements d'Avenir program, project ISITE-BFC (Contract ANR-15-IDEX-03).

[1] E. Yablonovitch, Inhibited Spontaneous Emission in Solid-State Physics and Electronics, Phys. Rev. Lett. **58**, 2059 (1987).
[2] K. Busch, G. von Freymann, S. Linden, S. F. Mingaleev, L. Tkeshelashvili, and M. Wegener, Periodic nanostructures for photonics, Phys. Rep. **444**, 101 (2007).
[3] A. Frölich, T. Fischer, J. Zebrowski, K. Busch, and M. Wegener, Titania woodpiles with complete three-dimensional photonic bandgaps in the visible, Adv. Mater. **25**, 3588 (2013).
[4] M. S. Kushwaha, P. Halevi, L. Dobrzynski, and B. Djafari-Rouhani, Acoustic Band Structure of Periodic Elastic Composites, Phys. Rev. Lett. **71**, 2022 (1993).
[5] R. V. Craster and S. Guenneau eds., *Acoustic Metamaterials: Negative Refraction, Imaging, Lensing and Cloaking*, Springer Series in Materials Science (Springer, Netherlands, 2013).
[6] V. Laude, *Phononic Crystals, Artificial Crystals for Sonic, Acoustic, and Elastic Waves* (De Gruyter, Berlin, Boston, 2015).
[7] M. Z. Hasan and C. L. Kane, Colloquium: Topological insulators, Rev. Mod. Phys. **82**, 3045 (2010).

[8] A. Lau, J. van den Brink, and C. Ortix, Topological mirror insulators in one dimension, Phys. Rev. B **94**, 165164 (2016).

[9] L. Lu, J. D. Joannopoulos, and M. Soljačić, Topological photonics, Nat. Phot. **8**, 821 (2014).

[10] R. Süsstrunk and S. D. Huber, Observation of phononic helical edge states in a mechanical topological insulator, Science **349**, 47 (2015).

[11] C. L. Kane and T. C. Lubensky, Topological boundary modes in isostatic lattices, Nat. Phys. **10**, 39 (2014).

[12] A. P. Schnyder, S. Ryu, A. Furusaki, and A. W. W. Ludwig, Classification of topological insulators and superconductors in three spatial dimensions, Phys. Rev. B **78**, 195125 (2008).

[13] A. Kitaev, Periodic table for topological insulators and superconductors, AIP Conf. Proc. **1134**, 22 (2009).

[14] R. Süsstrunk and S. D. Huber, Classification of topological phonons in linear mechanical metamaterials, Proc. Natl. Acad. Sci. USA **113**, E4767 (2016).

[15] F. D. M. Haldane and S. Raghu, Possible Realization of Directional Optical Waveguides in Photonic Crystals with Broken Time-Reversal Symmetry, Phys. Rev. Lett. **100**, 013904 (2008).

[16] Z. Wang, Y. Chong, J. D. Joannopoulos, and M. Soljačić, Observation of unidirectional backscattering-immune topological electromagnetic states, Nature **461**, 772 (2009).

[17] Y. Poo, R.-X. Wu, Z. Lin, Y. Yang, and C. T. Chan, Experimental Realization of Self-Guiding Unidirectional Electromagnetic Edge States, Phys. Rev. Lett. **106**, 093903 (2011).

[18] M. Hafezi, E. A. Demler, M. D. Lukin, and J. M. Taylor, Robust optical delay lines with topological protection, Nat. Phys. **7**, 907 (2011).

[19] Y. Wu, C. Li, X. Hu, Y. Ao, Y. Zhao, and Q. Gong, Applications of topological photonics in integrated photonic devices, Adv. Opt. Mater. **5**, 1700357 (2017).

[20] A. B. Khanikaev, R. Fleury, S. H. Mousavi, and A. Alù, Topologically robust sound propagation in an angular-momentum-biased graphene-like resonator lattice, Nat. Commun. **6**, 8260 (2015).

[21] S. H. Mousavi, A. B. Khanikaev, and Z. Wang, Topologically protected elastic waves in phononic metamaterials, Nat. Commun. **6**, 8682 (2015).

[22] R. Fleury, A. B. Khanikaev, and A. Alù, Floquet topological insulators for sound, Nat. Commun. **7**, 11744 (2016).

[23] K. V. Klitzing, G. Dorda, and M. Pepper, New Method for High-Accuracy Determination of the Fine-Structure Constant Based on Quantized Hall Resistance, Phys. Rev. Lett. **45**, 494 (1980).

[24] D. J. Thouless, M. Kohmoto, M. P. Nightingale, and M. den Nijs, Quantized Hall Conductance in a Two-Dimensional Periodic Potential, Phys. Rev. Lett. **49**, 405 (1982).

[25] M. V. Berry, Quantal phase factors accompanying adiabatic changes, Proc. Phys. Soc. London, Sec. A **392**, 45 (1984).

[26] J. Zak, Berry's Phase for Energy Bands in Solids, Phys. Rev. Lett. **62**, 2747 (1989).

[27] W. P. Su, J. R. Schrieffer, and A. J. Heeger, Soliton excitations in polyacetylene, Phys. Rev. B **22**, 2099 (1980).

[28] A. C. Eringen, *Microcontinuum Field Theories: I. Foundations and Solids*, Microcontinuum Field Theories (Springer Science & Business Media, New York, 1999).

[29] C. N. LaFratta, J. T. Fourkas, T. Baldacchini, and R. A. Farrer, Multiphoton fabrication, Angew. Chem. Int. Ed. **46**, 6238 (2007).

[30] G. von Freymann, A. Ledermann, M. Thiel, I. Staude, S. Essig, K. Busch, and M. Wegener, Three-dimensional nanostructures for photonics, Adv. Func. Mater. **20**, 1038 (2010).

[31] T. Frenzel, M. Kadic, and M. Wegener, Three-dimensional mechanical metamaterials with a twist, Science **358**, 1072 (2017).

[32] A. Sommerfeld, *Mechanics of Deformable Bodies,*, Lectures on Theoretical Physics Vol. 2 (Academic Press, Inc., New York, NY, 1950).

[33] H. Zhu, J. Yi, M.-Y. Li, J. Xiao, L. Zhang, C.-W. Yang, R. A. Kaindl, L.-J. Li, Y. Wang, and X. Zhang, Observation of chiral phonons, Science **359**, 579 (2018).

[34] M. Xiao, G. Ma, Z. Yang, P. Sheng, Z. Q. Zhang, and C. T. Chan, Geometric phase and band inversion in periodic acoustic systems, Nat. Phys. **11**, 240 (2015).

[35] R. Chaunsali, A. Thakkar, E. Kim, P. G. Kevrekidis, and J. Yang, Demonstrating an *in-situ* topological band transition in cylindrical granular chains, arXiv:1702.04756 [cond-mat, physics:nlin] (2017).

[36] I. Kim, S. Iwamoto, and Y. Arakawa, Topologically protected elastic waves in one-dimensional phononic crystals of continuous media, Appl. Phys. Express **11**, 017201 (2017).

[37] J. Yin, M. Ruzzene, J. Wen, D. Yu, L. Cai, and L. Yue, Band transition and topological interface modes in 1D elastic phononic crystals, Sci. Rep. **8**, 6806 (2018).

[38] Y. T. Wang, X. N. Liu, R. Zhu, and G. K. Hu, Wave propagation in tunable lightweight tensegrity metastructure, Sci. Rep. **8**, 11482 (2018).

[39] A. H. Orta and C. Yilmaz, Inertial amplification induced phononic band gaps generated by a compliant axial to rotary motion conversion mechanism, J. Sound Vib. **439**, 329 (2018).

[40] M. Xiao, Z. Q. Zhang, and C. T. Chan, Surface Impedance and Bulk Band Geometric Phases in One-Dimensional Systems, Phys. Rev. X **4**, 021017 (2014).

[41] A. Altland and M. R. Zirnbauer, Nonstandard symmetry classes in mesoscopic normal-superconducting hybrid structures, Phys. Rev. B **55**, 1142 (1997).

[42] Y. Barlas and E. Prodan, Topological classification table implemented with classical passive metamaterials, Phys. Rev. B **98**, 094310 (2018).

[43] X.-L. Qi and S.-C. Zhang, Topological insulators and superconductors, Rev. Mod. Phys. **83**, 1057 (2011).

[44] C.-K. Chiu, Y.-H. Chan, and A. P. Schnyder, Quantized Berry Phase and Surface States under Reflection Symmetry or Space-Time Inversion Symmetry, arXiv:1810.04094 [cond-mat] (2018).